JOURNAL OF PROPULSION AND POWER
Vol. 20, No. 1, January–February 2004

Three-Dimensional Time-Resolved Inlet Guide Vane–Rotor Potential Field Interaction

Robert T. Johnston* and Sanford Fleeter†
Purdue University, West Lafayette, Indiana 47907

To investigate and quantify the three-dimensional time-varying characteristics of inlet guide vane (IGV) wakes, including the effect of the potential field of a downstream rotor, a series of experiments are performed in a high-speed fan stage. The unsteady three-dimensional velocity and total pressure fields downstream of the IGVs and upstream of the rotor have been measured across one vane passage and time resolved over several rotor blade passage periods. These unique data will be compared with several wake correlations and analyzed to determine the time-varying characteristics of the IGV wakes. Earlier two-component velocity measurements identified a unique interaction occurring between the rotor potential field and the IGV wakes. The rotor potential field increases as the IGV wakes approach the rotor, resulting in a constructive/destructive interaction. Measurements of the IGV wake at times of maximum and minimum interaction show that the constructive interaction increases the velocity deficit and semiwake width as the distance from the rotor decreases. A two-dimensional vortical–potential gust splitting analysis will be implemented to determine the vortical and potential harmonic wake gust forcing functions upstream of the rotor over one rotor blade passing period.

Nomenclature

A_n	=	potential disturbance nth harmonic constant
C_I	=	inlet guide vane (IGV) chord
C_R	=	rotor chord
c_0	=	speed of sound
D_n	=	vortical disturbance nth harmonic constant
$\boldsymbol{k}$	=	gust wave number vector
M	=	Mach number
p	=	static pressure perturbation
S_I	=	IGV spacing at midspan
S_R	=	rotor blade spacing at midspan
$\bar{\boldsymbol{U}}$	=	mean absolute velocity vector
$\boldsymbol{U}$	=	absolute velocity vector
u	=	axial velocity perturbation
v	=	tangential velocity perturbation
$\bar{\boldsymbol{W}}$	=	mean IGV-relative velocity vector
W_{dc}	=	wake streamwise centerline velocity defect
W_0	=	free stream streamwise velocity
$\boldsymbol{w}$	=	perturbation velocity vector
$\boldsymbol{w}_{pn}$, $\boldsymbol{w}_{vn}$	=	nth harmonic potential and vortical gusts
$\boldsymbol{x}$	=	axial and tangential spatial coordinates, $\xi_{e_\xi} + \eta_{e_\eta}$
z	=	axial IGV-to-rotor spacing at midspan
$\bar{\alpha}$	=	absolute flow angle
δ	=	semi wake width
ϕ	=	potential function
ξ_u, ξ_d	=	axial distance upstream and downstream of the rotor

Subscripts

I	=	IGV
m	=	measured
p	=	potential
R	=	rotor
v	=	vortical

Received 16 August 2003; revision received 5 June 2003; accepted for publication 13 June 2003.

*School of Mechanical Engineering; currently Development Instrumentation Technology Mgr, Pratt and Whitney. Member AIAA.

†McAllister Distinguished Professor, School of Mechanical Engineering. Fellow AIAA.

Introduction

BLADE row–wake interactions are the most common and least understood source of unsteady aerodynamic excitation and cause blade row vibrations that result in high-cycle blade fatigue. Modern turbomachines are designed with closely spaced blade rows to reduce weight. As a result, the value of traditional wake forcing function models for forced response prediction is significantly limited. First, currently used wake forcing function empirical or semi-empirical models have been based on far-wake steady flow measurements from a single isolated airfoil row, often operated in the incompressible flow regime. Hence, these far-field wake data are not appropriate for closely spaced compressible Mach number blade rows. Second, the airfoil row generates a potential field due to its thickness and lifting properties in addition to a viscous wake. This potential field decays rapidly with distance but is significant for closely spaced blade rows.

Forced response predictions are based on linearized two-dimensional inviscid cascade analyses. First, a definition of the unsteady aerodynamic wake forcing function in terms of its harmonics is required. The unsteady aerodynamic response of the downstream blade row to each wake harmonic is then analyzed. These gust forcing functions consist of potential and vortical components. Potential disturbances extend both upstream and downstream, decay exponentially with distance in subsonic flow, and would exist in the absence of viscosity. Vortical wakes convect downstream with the mean flow and result from viscous action at the blade surface. If the flow were inviscid, these vortical wakes would remain constant with time.

This linearized approach to forced response prediction typically considers an isolated blade row. Thus, multistage blade row interaction effects on the forcing function are neglected. However, such blade row interactions give rise to many significant phenomenon. For example, a stator vane wake positioned in the deficit of an upstream stator has a larger deficit than if it were positioned between the upstream generated stator wakes. Rotor blade wake velocity deficits decrease in the region of an upstream stator velocity deficit.[1,2] This phenomenon can be exploited to effect a reduction in sound level at blade passage frequency. Huber et al.[3] investigated the performance improvements achievable by circumferentially indexing successive rows of turbine stator rows. The peak efficiency was found to occur when the wake from the first vane row impinged on the second vane after passing through a rotor, whereas the minimum efficiency is found when the first vane row wake passes between the

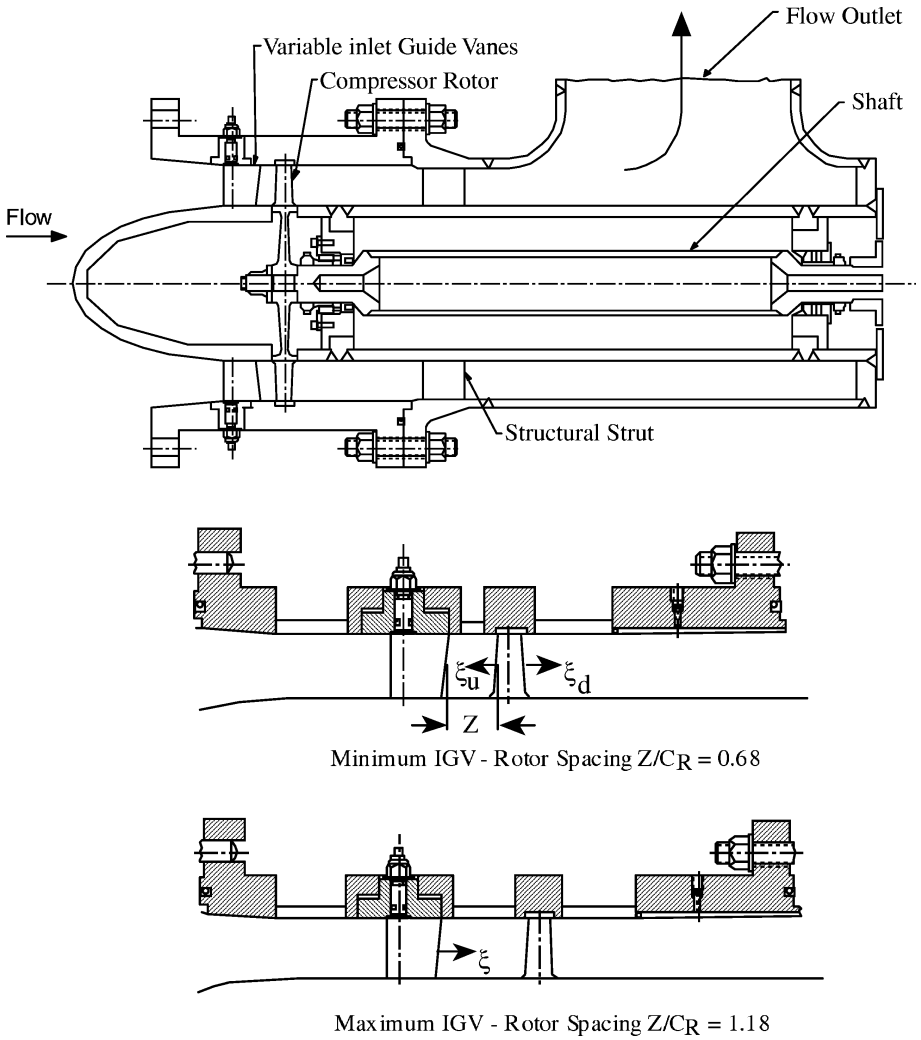

Fig. 1 Research fan stage test section cross section and spacing detail.

second-stage vanes. A model to predict vane row indexing as a passive vibration control technique has also been developed.[4] Correctly indexing stationary airfoil rows was shown to reduce significantly aerodynamic lift and moment even when the axial spacing was small.

The facility used for the experimental investigation consists of an inlet guide vane (IGV) row and a high-speed rotor and is ideal for the quantitative investigation of wake forcing functions because it is large enough for the necessary high-quality measurements, the IGV-rotor axial spacing is variable, and the IGV row can be indexed circumferentially, thereby enabling IGV wakes to be measured with stationary probes. The rotor is 30.48 cm in diameter and has 2/3 hub–tip ratio. There are 18 inlet guide vanes, which introduce swirl into a 19-blade axial flow rotor.

To predict accurately flow-induced vibrations of blade rows in a multistage environment, thereby also making passive rotor vibration control techniques such as vane row indexing practical, a quantitative understanding of the time-varying characteristics of wakes interacting with downstream blade rows is required. Data have been acquired that allow the interaction between the IGV wakes with a rotor potential field to be analyzed as a function of rotor position. Furthermore, these data allow the rotor potential field as a function of position relative to the wake to be assessed. Further analysis of these unique data sets would yield a greater understanding of the unsteady nature of aerodynamic forcing functions due to blade row interactions.

Axial Fan Facility

The Purdue University Research Axial Fan facility features a 30.48 cm (12 in.) diameter, 2/3 hub–tip ratio design compressor rotor which is integral with the shaft. The drive system consists of a 400-hp (298.3 kW) ac motor driving a magnetic clutch with a variable speed output, which drives a gearbox. Figure 1 shows the 18 IGVs that introduce swirl into a 19-blade axial flow rotor. The IGVs and rotor blades have NACA 65 series profiles on circular arc meanlines. The adjustable IGVs have a nominal 10% thickness with a chord varying from 35.5 mm (1.40 in.) at the hub to 53.3 mm (2.10 in.) at the tip to yield a solidity of one. IGV twist distribution produces a free-vortex whirl into the rotor. Rotor blade sections have a 10–6% hub-to-tip thickness taper, with a chord of 50.8 mm (2.00 in.). For this experiment, an axial IGV-to-rotor spacing to chord ratio of 60% ($Z/C_R = 0.6$) is investigated. Axial IGV-to-rotor spacing is dependent on IGV stagger angle, which was set to 10 deg for these tests. The IGV row is indexed circumferentially, thereby enabling the IGV wake measurements to be made without circumferential probe traverses upstream and downstream of the rotor. Axial distance downstream of the IGV trailing edge at midspan is ξ, and the axial distance upstream of the rotor leading edge is ξ_u. The compressor is operated at 16,000 rpm for all tests, giving an IGV exit Mach number of 0.42 and typical mass flow rates of 5.35 kg/s.

Data Acquisition and Instrumentation

At each circumferential location, the velocity and total pressure are measured downstream of the IGV row to determine the IGV wake steady and unsteady characteristics. The measurements are taken in 1.0-deg increments in the freestream region and in 0.2-deg increments in the wake region. The wake regions are identified by first taking a traverse of one IGV passage with the coarse

circumferential increments. Then the wake region is resolved by taking measurements at smaller increments across the wake. Time–mean signals at each IGV azimuthal location are determined by taking the average of measurements of 80 rotor revolutions sampled at 1900 points per revolution. At each of these azimuthal locations, the time-varying or unsteady velocity and total pressure are also measured. The time-variant signals are digitized over 10 blade passages using approximately 1000 samples per burst and are ensemble averaged over 100 individual revolutions, triggered by a once-per-revolution pulse from a photooptic sensor. These time-resolved velocity and total pressure data are then used to calculate the static pressure assuming the flow is isentropic.

Midspan time-variant velocity and total pressure data are acquired downstream of the IGV with hot-film anemometers and unsteady total pressure probes designed to access the confined regions upstream of the rotor. An Endevco piezoresistive pressure transducer with a sensitivity of 59.85 mV/psi and a frequency response of 70 kHz is installed in a stainless-steel probe body. This design is capable of $\pm$17-deg misalignment to the flow with less than 1% error in total pressure. The unsteady rotor wake three-component velocity data are acquired with a slant hot-film anemometer with a measurement area of 50.8 μm $\times$ 1.0 mm.

Three components of velocity are measured by rotating the single slant wire to four separate angles about the probe axis. Signals from the four angular positions yield four combinations of three signals. In brief, the three components of velocity are determined using a Newton–Raphson numerical technique from the measured signals at three angular positions to determine the velocity V, the yaw angle θ_y, and the pitch angle θ_p. The advantage of this method is that redundant measurements are available in the event that a particular combination fails to converge to a reasonable solution. Measurements at each probe orientation are ensemble averaged and stored to disc along with the rms of the ensemble averaged voltage signal. These data provide for the evaluation of the ensemble-averaged flowfield and the rms velocity of this ensemble-averaged signal.

The rotor relative inlet midspan Mach number is 0.42. Hence, for these rotor wake experiments, with data acquired in the absolute reference frame, a compressible hot-wire calibration technique is necessary. Velocity calibration data are acquired with the wire oriented at 90 deg to the calibration jet and over a range of appropriate velocities. These data are analyzed to determine the coefficients A and B in the following Kings law equation, which relates the wire voltage E to the effective cooling velocity V_{eff} and the thermal conductivity of air k_f. The effective voltage is corrected for changes in density of the flow in the compressor. This compressible calibration method is detailed by Johnston and Fleeter.[5] Thus,

$$E^2 = \left(BV_{\text{eff}}^{0.5} + Ak_f\right)(T_w - T_f) \tag{1}$$

Calibration data are acquired and analyzed over a range of Mach numbers from 0.25 to 0.5, over a range of pitch angles from -20 to $+20$ deg, and over yaw angles from -70 to 70 deg. The b_n coefficients in the velocity calibration

$$V_e/V = b_0 + b_1\alpha_s + b_2\theta_p + b_3V + b_4\alpha_s^2 + b_5\theta_p^2 + b_6V^2 + b_7\alpha_s\theta_p + b_8\alpha_sV + b_9\theta_pV \tag{2}$$

are determined by a least-squares curve fit of the calibration data.[6] A comparison of the velocity calculated from the curve fit to the calibration data yields less than 2% difference for 78% of the 758 points taken, with the remaining 22% of the data points having between 2 and 4% differences from the curve fit. These differences between the calibration data and the polynomial curve can be further reduced by selecting smaller ranges over which to fit the data, but significantly increasing the processing time required by the Newton–Raphson solver.

Because the unsteady measurements are all initiated at the same rotor blade position for all IGV positions, the data are shifted in time to account for rotor blade position (Fig. 2). For measurements behind the trailing edge of vane I1, data acquisition is initiated when the leading edge of rotor blade R1 passes the measuring point.

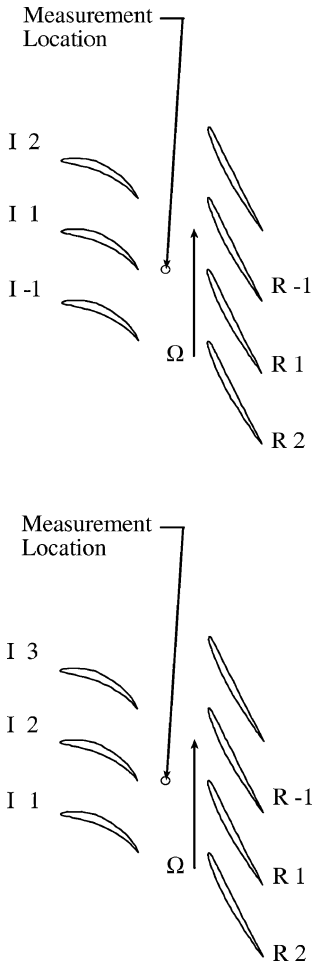

Fig. 2 Vane clocking and data processing schematic at start of data acquisition: initial position and vanes clocked one IGV passage.

When I2 is upstream of the measurement location, the unsteady data acquisition is again initiated when R1 passes the probe. Thus, all locations, with the exception of the last azimuthal location, are time shifted by an amount proportional to the radial location and angular position relative to the final point and inversely proportional to the wheel speed.

Wake Velocity and Semiwake Width Correlations

The physical features of the time-averaged IGV wakes are characterized by measuring the semiwake width δ and the wake centerline velocity defect W_{dc} (Fig. 3). Numerous empirical correlations have been made for these two quantities, which quantify the physical nature of the wakes, and several have been selected for comparison to the experimental results. All equations have been rewritten using the notation of Majjigi and Gliebe.[7] For this particular fan stage, the IGV spacing is equal to the chord at all radial locations. Therefore, the two are used interchangeably in the following equations.

Majjigi and Gliebe Correlation[7]

The Majjigi and Gliebe[7] correlation equations are

$$\frac{\delta}{C_I} = \frac{0.2375(s/C_I)C_D^{0.125} + 0.034125}{0.357(s/C_I)C_D^{0.125} + 1.0}$$

$$\frac{W_{dc}}{W_0} = C_D^{0.25}\frac{0.3675(s/C_I) + 1.95}{7.65(s/C_I) + 1.0} \tag{3}$$

where s is the streamwise distance from the IGV trailing edge, C_D is the airfoil section drag coefficient, and W_{dc} and W_0 are the wake centerline velocity defect and freestream velocity, respectively.

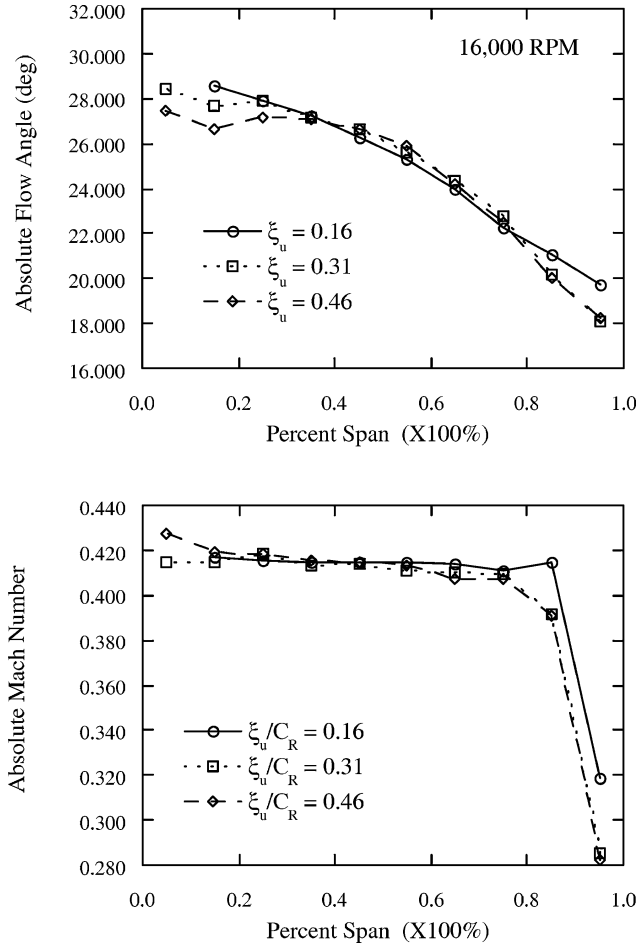

Fig. 3 Absolute flow angle and absolute Mach number for three axial positions.

A modified Majjigi and Gliebe correlation[7] that uses a drag coefficient that is 20% of that shown was found to yield good agreement with the IGV wake velocity deficit and semiwake width.[8] This value was chosen because it was found to give good agreement to the data from this compressor.

Lakshminarayana and Davino Correlation

The Lakshminarayana and Davino[9] correlation equations for the near wake ($0.06 < \xi/C_I < 0.4$) are

$$\delta/C_I = (1.39/2)C_D^{0.5}\left(sC_I^{-1}\cos\alpha + 0.55\right)^{1.22}$$

$$\frac{W_{dc}}{W_0} = C_D^{0.5}\frac{1.68}{\left(sC_I^{-1}\cos\alpha + 0.12\right)^{0.22}} + C_D^{0.5}\frac{0.353}{\left(sC_I^{-1}\cos\alpha + 0.12\right)^{1.22}} \tag{4}$$

and for the far wake ($\xi/C_I > 0.4$), the correlation equations are

$$\frac{\delta}{C_I} = \frac{1.18}{2}C_D^{0.5}\left(sC_I^{-1}\cos\alpha + 0.688\right)$$

$$\frac{W_{dc}}{W_0} = C_D^{0.5}\frac{0.9792}{\left(sC_I^{-1}\cos\alpha + 0.688\right)} \tag{5}$$

Vortical–Potential Gust Splitting Analysis

The two-dimensional inviscid flow is assumed to be compressible, isentropic, and composed of an absolute mean velocity $\bar{\boldsymbol{U}}$ with superimposed small velocity $\boldsymbol{w}$ and static pressure spatial perturbations p (Feiereisen and Fleeter[10]). The linearized continuity and momentum equations are

$$\frac{1}{c_0^2}\frac{\bar{\mathrm{D}}p}{\mathrm{D}t} + \bar{\rho}\nabla\cdot\boldsymbol{w} = 0, \qquad \bar{\rho}\frac{\bar{\mathrm{D}}\boldsymbol{w}}{\mathrm{D}t} + \nabla p = 0 \tag{6}$$

Vortical–Potential Splitting

The perturbation velocity field is split into vortical and potential gust components that satisfy

$$\frac{\bar{\mathrm{D}}\boldsymbol{w}_v}{\mathrm{D}t} = 0, \qquad \nabla\cdot\boldsymbol{w}_v = 0 \tag{7}$$

$$\rho\frac{\bar{\mathrm{D}}\boldsymbol{w}_p}{\mathrm{D}t} = -\nabla_p, \qquad \frac{1}{\rho c_0^2}\frac{\bar{\mathrm{D}}p}{\mathrm{D}t} = -\nabla\cdot\boldsymbol{w}_p, \qquad \nabla\times\boldsymbol{w}_p = 0 \tag{8}$$

Thus, the forcing function is analyzed harmonically as a Fourier series of individual vortical and potential gusts,

$$\boldsymbol{w}\langle\boldsymbol{x}, t\rangle = \sum_{n=0}^{\infty}\langle\boldsymbol{w}_{vn}\langle\boldsymbol{x}\rangle + \boldsymbol{w}_{pn}\langle\boldsymbol{x}\rangle\rangle e^{in\omega t}$$

Vortical Gust

The vortical gust is satisfied by a function that is periodic in the axial and tangential directions. The complex constant of proportionality, which characterizes the magnitude of the vortical gust, is D_n^*.

$$\boldsymbol{w}_{vn} = D_n^*\bar{U}\left(\cos\bar{\alpha}_{e_\xi} + \sin\bar{\alpha}_{e_\eta}\right)\exp(-\mathrm{in}\boldsymbol{k}\cdot\boldsymbol{x}) \tag{9}$$

Thus, the vortical gust propagates unattenuated in the direction of the gust wave number vector $\boldsymbol{k}$. This defines the vortical gust velocity perturbation with all parameters known from measurements with the exception of D_n^*, which must be calculated for each harmonic.

Potential Gust

The potential gust $\boldsymbol{w}_p$ must satisfy $\nabla\times\boldsymbol{w}_p = 0$ and, therefore, can be derived from a potential function, $\boldsymbol{w}_p = \nabla\phi_p$. The perturbation potential is related to the pressure perturbation p through the unsteady Bernoulli equation. Substituting these relations into Eq. (6) yields the following perturbation velocity potential equation:

$$\frac{1}{c_0^2}\frac{\bar{\mathrm{D}}}{\mathrm{D}t}\left(\frac{\bar{\mathrm{D}}\phi_p}{\mathrm{D}t}\right) - \nabla^2\phi_p = 0 \tag{10}$$

Because the flow is steady, the potential gust solution, determined from the steady form of this equation, is

$$\phi_{pn} = A_n\exp\{n(\chi k_\eta\xi - ik_\eta\eta)\} \tag{11}$$

where

$$\chi = \frac{-iM^2\sin\bar{\alpha}\cos\bar{\alpha} \pm \sqrt{1-M^2}}{1 - M^2\cos^2\bar{\alpha}}$$

is the axial decay factor and A_n is a complex constant.

Thus, the potential gust is spatially periodic in the tangential direction but decays exponentially in the axial direction (except in a cut-on condition). The direction of this axial decay depends on whether an upstream or downstream blade row is being analyzed. The potential static pressure perturbation is found from the unsteady Bernoulli equation:

$$p_{pn}/\rho\bar{U}^2 = A_n^*(-\chi\cos\bar{\alpha} + i\sin\bar{\alpha})\exp\{n(\chi k_\eta\xi - ik_\eta\eta)\} \tag{12}$$

Experimental Determination of D_n^* and A_n^*

The potential gust $\boldsymbol{w}_{pn}$ is irrotational. Therefore, the vorticity γ_{pn} is zero, $|\gamma_{pn}| = |\nabla\times\boldsymbol{w}_{pn}| = 0$, and P_{pn} is given in Eq. (15). Thus, the potential gust manifests itself in both static pressure and velocity spatial perturbations, but not in the vorticity perturbation. The vorticity of the vortical gust is

$$|\gamma_{vn}| = |\nabla\times\boldsymbol{w}_{vn}| = D_n^*(\mathrm{ink}_\eta\bar{U}/\cos\bar{\alpha})\exp(-in\boldsymbol{k}\cdot\boldsymbol{x})$$

and there is no corresponding static pressure perturbation. This vortical gust component, therefore, manifests itself in a vorticity perturbation, but not in the static pressure perturbation.

The spatial static pressure perturbation is dependent only on the potential gust. At the measurement location $(\xi, \eta) = (0, 0)$, the potential gust coefficient A_n^*, computed explicitly from the calculated static pressure, is

$$A_n^* = p_{mn}/\rho\bar{U}^2(-\chi\cos\bar{\alpha} + i\sin\bar{\alpha}) \tag{13}$$

where p_{mn} is the measured nth harmonic static pressure spatial perturbation.

The potential gust velocity perturbation is then calculated and subtracted from the measured velocity perturbation to yield a difference velocity perturbation. Because the vorticity of the potential component is zero, the perturbation of the velocity difference has the same vorticity as the measured gust. Thus, the linear theory vortical gust coefficient is calculated from this difference velocity perturbation as

$$A_n^* = p_{mn}/\rho\bar{U}^2(-\chi\cos\bar{\alpha} + i\sin\bar{\alpha}) \tag{14}$$

Results

Time-resolved IGV wake data upstream of the rotor are acquired and analyzed for an IGV-rotor axial spacing of $Z/C_R = 0.6$, with an IGV outlet Mach number of 0.42 and a rotor relative inlet Mach number of 0.88 at midspan. Measurements of the semiwake width and velocity deficit using the time-averaged IGV wake data are compared to several existing correlations. Analysis of the results of the two-dimensional vortical–potential splitting technique applied to the time-varying IGV wake, and the rotor potential field data are also presented.

Physical Characteristics of the Wakes

The absolute exit Mach number and flow angle out of the IGV are shown in Fig. 3 as a function of spanwise location. At midspan the Mach number is 0.42 and the turning angle is 25.8 deg. Operational speed was 16,000 rpm, and it was chosen because the flow on the rotor blades was known to be attached and the rotor blade operation was transonic. Pressure sensitive paint measurements[11] were performed at a range of speeds, and the presence of a shock was detected at approximately 60% chord at this operational speed.

Figures 4–6 show the mean, minimum, and maximum velocity as a function of IGV blade passage for the downstream locations $\xi = 0.16, 0.36$, and 0.52 at midspan. The difference of the maximum and minimum velocity profiles increases, as expected, as the rotor blades are approached due to the increasing rotor potential field. Plotting the difference between the maximum and minimum curves shows that the velocity perturbations increase in the region of the

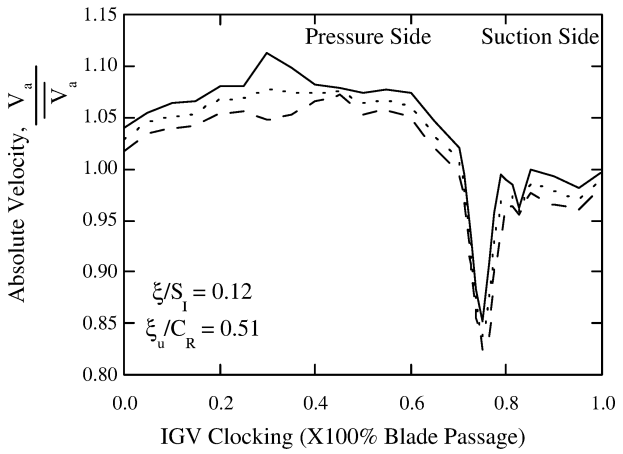

Fig. 4 Time-averaged absolute velocity at station closest to IGV, $\zeta/S_I = 0.12$: ——, maximum absolute velocity; - - - -, average absolute velocity; and – – –, minimum absolute velocity.

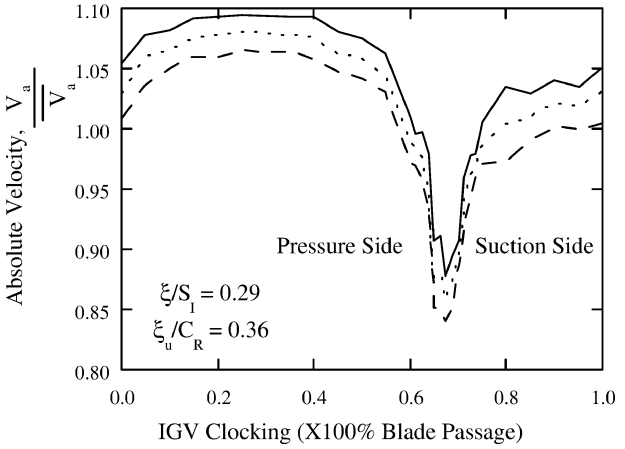

Fig. 5 Time-averaged absolute velocity at station 2, $\zeta/S_I = 0.29$: ——, maximum absolute velocity; - - - -, average absolute velocity; and – – –, minimum absolute velocity.

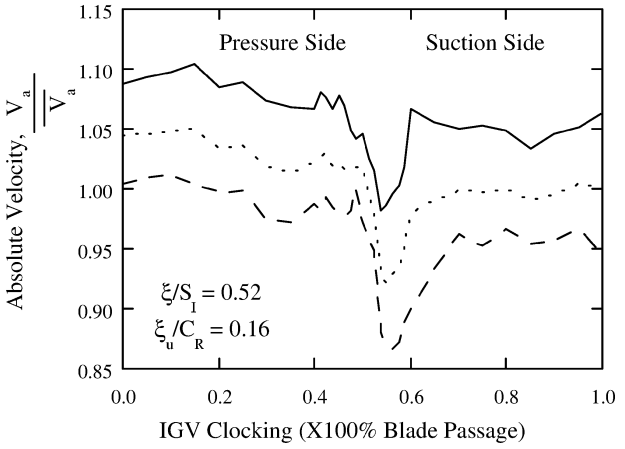

Fig. 6 Time-averaged absolute velocity at station 4, $\zeta/S_I = 0.52$: ——, maximum absolute velocity; - - - -, average absolute velocity; and – – –, minimum absolute velocity.

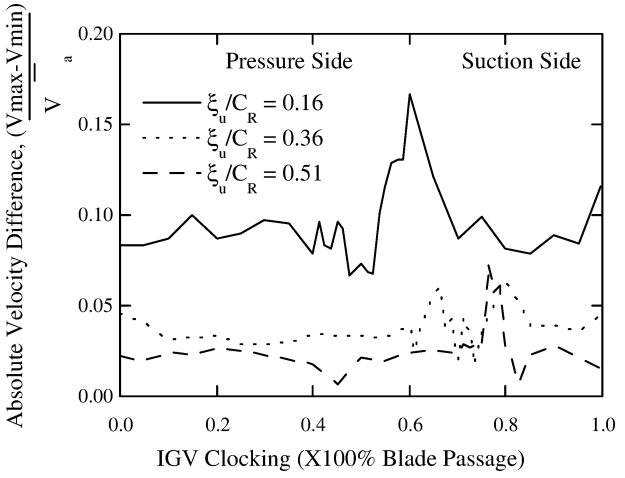

Fig. 7 Difference velocity across IGV wake.

IGV wake. This is attributed to the effect of the rotor wake chopping the IGV wake. When the rotor blades cut the IGV wake, there are large unsteady pressure fluctuations on the rotor blade, which lead changes in the upstream rotor potential. The difference velocity is shown in Fig. 7.

The extreme positions of the axial, tangential, and radial velocity distributions at the station closest to the rotor, $\xi = 0.52$ (Figs. 8–10). The velocity profile, which increases the effect of the wake in

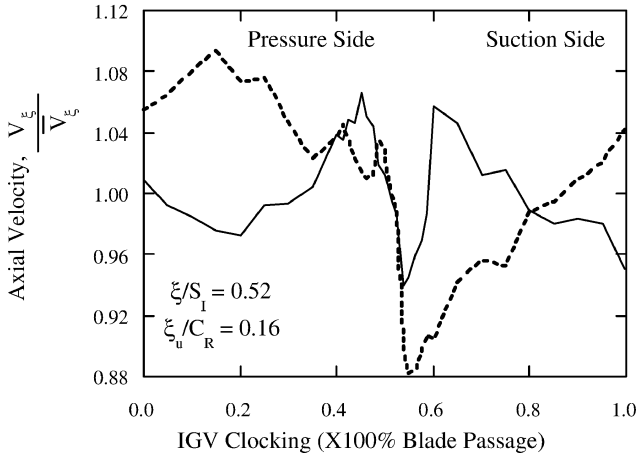

Fig. 8 Axial velocity fluctuations: ——, destructive interaction and - - - -, constructive interaction.

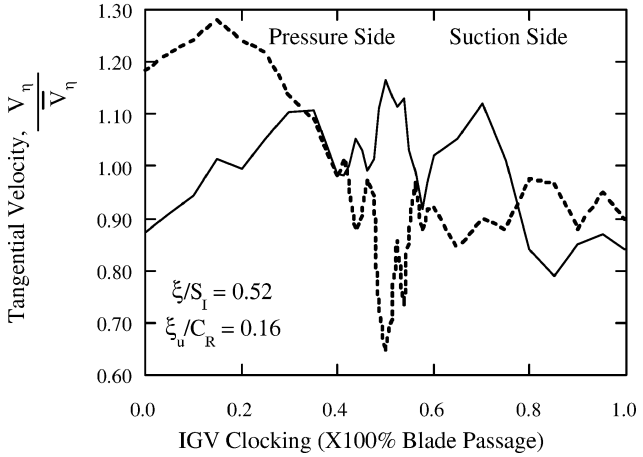

Fig. 9 Tangential velocity fluctuations: ——, destructive interaction and - - - -, constructive interaction.

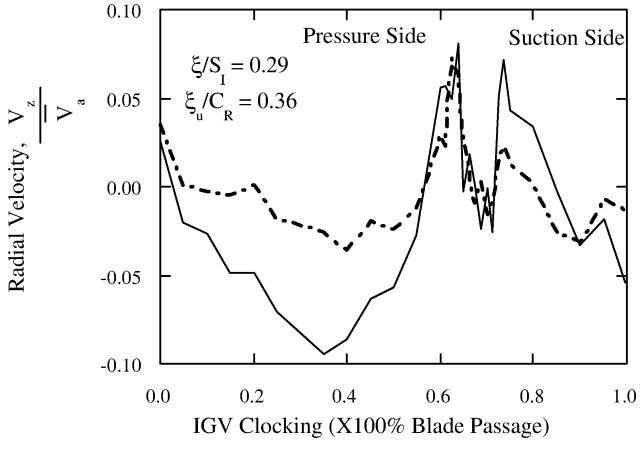

Fig. 10 Radial velocity fluctuations: ——, constructive interaction and –·–, destructive interaction.

Figs. 8–10 is called the constructive interaction condition, although this does not mean that these profiles occur simultaneously. In Fig. 8, the axial velocity deficit increases dramatically when the constructive interaction occurs. When the tangential velocity profile is examined, we can see that there is considerable overturning outside the IGV wake and underturning in the IGV wake for the constructive interaction. When the destructive interaction occurs in the tangential velocity profile, there is overturning in the wake region and underturning between the wakes. Figure 10 shows the radial velocity profiles. Note that the flow in the wake region is always toward the hub. This radially inward flow is a result of an imbalance of the centrifugal and pressure forces near the surface of the blade. The constructive interaction of the radial velocity occurs 180-deg out-of-phase with the constructive interaction in the axial and tangential velocity profiles.

Total pressure profiles downstream of the IGV are shown at three locations at the extreme conditions (Figs. 11–13). Note that the total

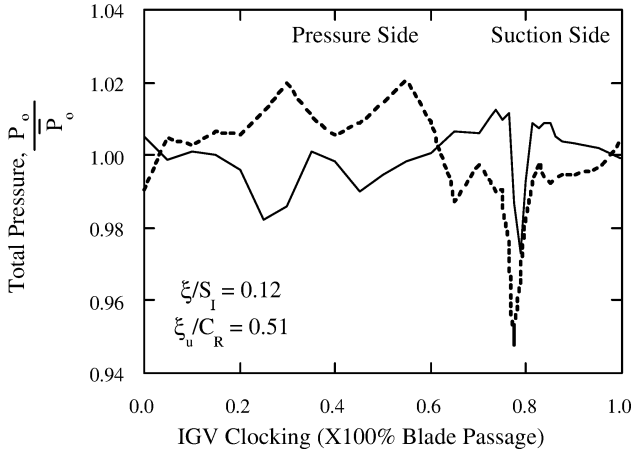

Fig. 11 Total pressure fluctuations at station nearest IGV: ——, destructive interaction and - - - -, constructive interaction.

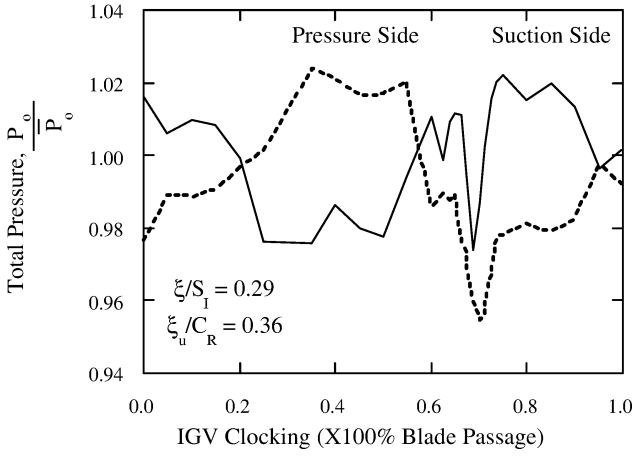

Fig. 12 Total pressure fluctuations at second station: ——, destructive interaction and - - - -, constructive interaction.

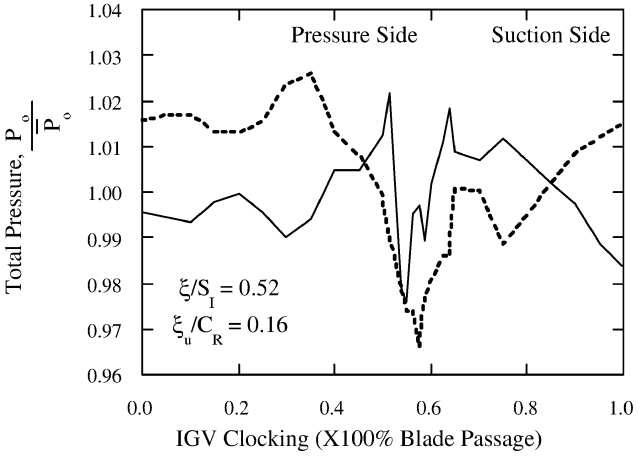

Fig. 13 Total pressure fluctuations at station nearest the rotor: ——, destructive interaction and - - - -, constructive interaction.

pressure losses in the IGV wakes is maximized for the constructive interaction. This effect increases as the rotor blades are approached.

IGV wake velocity deficit and semiwake width are measured and compared to the correlations presented earlier. The semiwake width for the time-averaged and destructive interaction are in good agreement with each other and all three correlations (Fig. 14). Note that as the rotor is approached the semiwake width for the constructive interaction increases dramatically. The nature of the semiwake width for the axial velocity shown in Fig. 15 is similar in nature to that

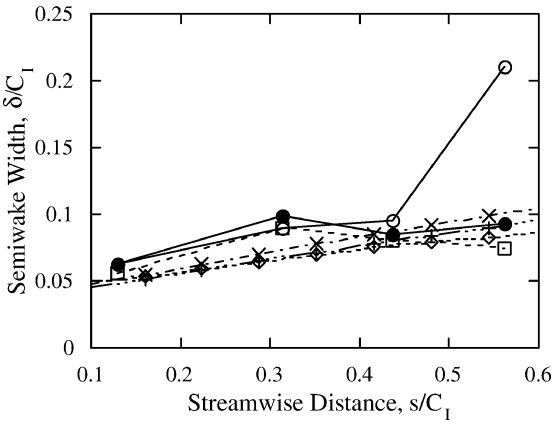

Fig. 14 IGV semiwake width measured from absolute velocity: ○, constructive interaction; ●, destructive interaction; □, time average; ×, Majjigi–Gliebe correlation[7]; +, modified Majjigi–Gliebe correlation; and ◇, Lakshminarayana–Davino.[9]

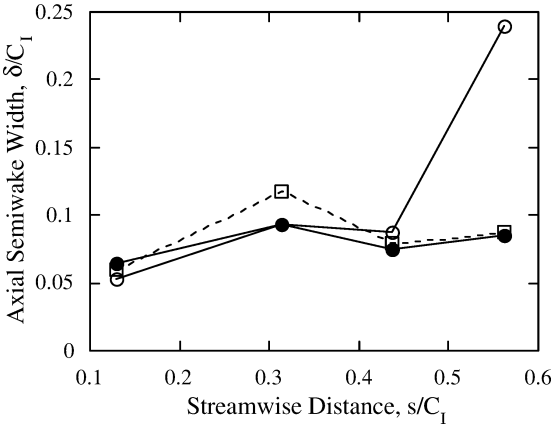

Fig. 15 IGV semiwake width measured from axial velocity: ○, constructive interaction; ●, destructive interaction; and □, time average.

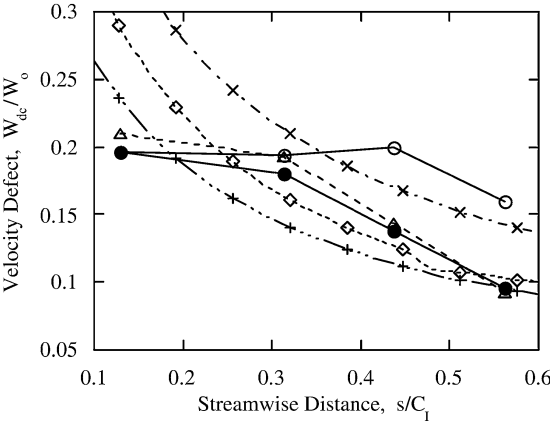

Fig. 16 IGV velocity deficit measured from absolute velocity: ○, constructive interaction; ●, destructive interaction; △, time-averaged results; ×, Majjigi–Gliebe correlation[7]; +, modified Majjigi–Gliebe correlation; and ◇, Lakshminarayana–Davino.[9]

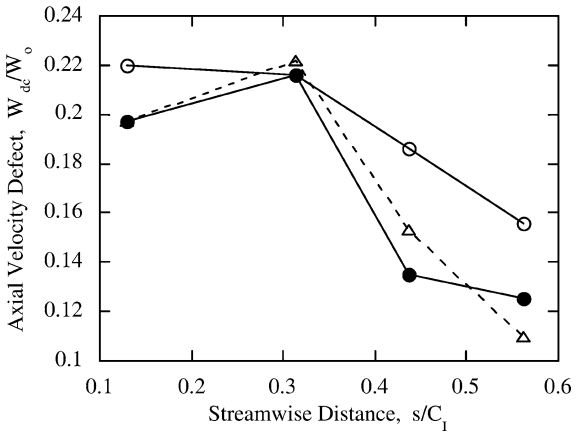

Fig. 17 IGV velocity deficit measured from axial velocity: ○, constructive interaction; ●, destructive interaction; and △, time-averaged results.

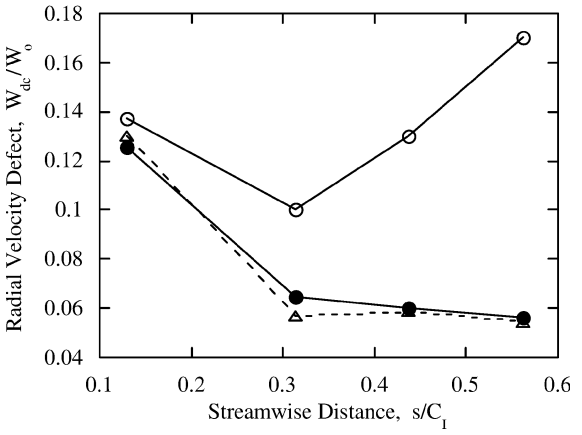

Fig. 18 IGV velocity deficit measured from radial velocity: ○, constructive interaction; ●, destructive interaction; and △, time-averaged results.

of the absolute velocity. The velocity deficit of the time-averaged and destructive interaction measured from the absolute velocity is in good agreement with the modified Majjigi-Gliebe correlation[7] and the Lakshminarayana and Davino correlation.[9] The constructive interaction leads to a large velocity deficit as the rotor is approached (Fig. 16). Figures 17–19 show the velocity deficit in the axial, radial, and tangential velocity profiles. In all three, the constructive interaction causes larger deficits than either the time-averaged or the destructive interaction. The radial velocity deficit is larger at all axial locations for the constructive interaction.

Results of the two-dimensional linear theory analysis applied to the time varying IGV wake are shown in Figs. 20 and 21. The potential gust first-harmonic magnitude goes through a complete cycle over one rotor blade pass period. This potential component increases as the rotor is approached due to the increasing magnitude of the rotor potential field. Similarly, the first-harmonic vortical gust magnitude completes one cycle during one rotor blade pass period. The maximum of each curve corresponds the constructive interaction and the minimum corresponds to the destructive interaction.

The splitting analysis was also applied to the rotor potential field, and the results are plotted up as a function of IGV clocking position in Figs. 22 and 23. Note that the rotor potential field is largest in the region of the IGV wakes, and this is attributed to the rotor blade surface pressure fluctuations, which occur as a result of the IGV wake being cut by the rotor blades. Note that the vortical component is much smaller than the vortical component of the time-varying IGV wake. This indicated that the interaction creates an increase in the apparent vortical component in the IGV wake, which can not be attributed to the rotor wake vortical component. To determine if this

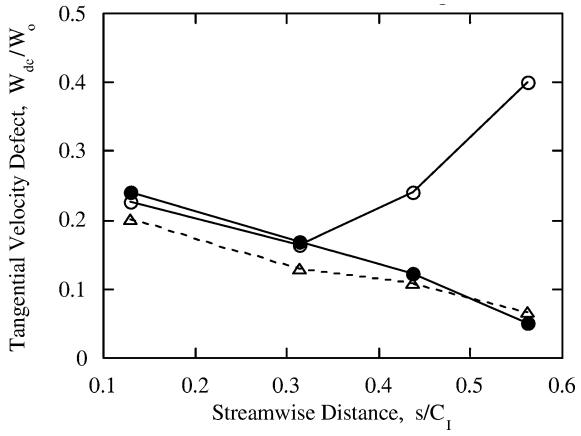

Fig. 19 IGV velocity deficit measured from tangential velocity: ○, constructive interaction; ●, destructive interaction; and △, time-averaged results.

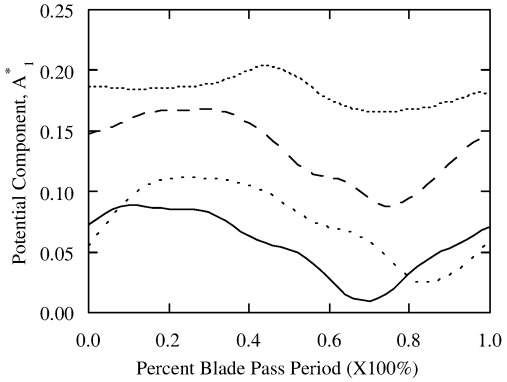

Fig. 20 Time-varying first-harmonic potential gust magnitude: ——, $A_1^*\xi/S_I = 0.16$; - - - -, $A_1^*\xi/S_I = 0.36$; – – –, $A_1^*\xi/S_I = 0.41$; and · · · ·, $A_1^*\xi/S_I = 0.52$.

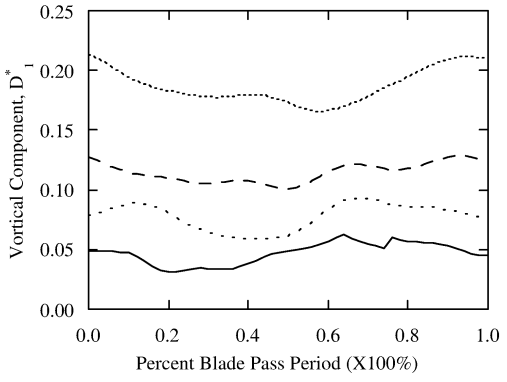

Fig. 21 Time-varying first-harmonic vortical gust magnitude: ——, $A_1^*\xi/S_I = 0.16$; - - - -, $A_1^*\xi/S_I = 0.36$; – – –, $A_1^*\xi/S_I = 0.41$; and · · · ·, $A_1^*\xi/S_I = 0.52$.

effect was consistent with other data, the analysis was applied to the unsteady IGV wake data presented previously in Ref. 8. These data were taken at lower Mach number, a higher IGV angle of attack, and for three different IGV–rotor blade spacings (IGV relative Mach number of 0.29). As in the high-speed results, there is a definite increase in the rotor blade potential field in the IGV wake region, and there is also an apparent increase in the vortical component in this region. These results were consistent with the results at the other spacings. If the acoustic interaction modes were accounted for in this analysis, the rotor vortical gust magnitude would be expected to be lower than it is at present. A three-component and/or acoustic splitting analysis is to be applied to this unique data set in the near future.

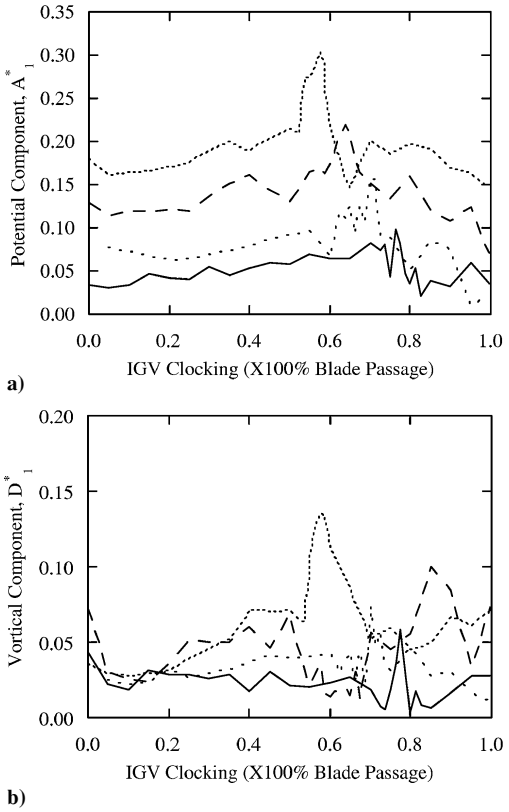

Fig. 22 Time-varying first-harmonic potential–vortical gust magnitude of the rotor: a) potential: ——, $A_1^*\xi/S_I = 0.16$; - - - -, $A_1^*\xi/S_I = 0.36$; – – –, $A_1^*\xi/S_I = 0.41$; and · · · ·, $A_1^*\xi/S_I = 0.52$ and b) vortical: ——, $A_1^*\xi/S_I = 0.16$; - - - -, $A_1^*\xi/S_I = 0.36$; – – –, $A_1^*\xi/S_I = 0.41$; and · · · ·, $A_1^*\xi/S_I = 0.52$.

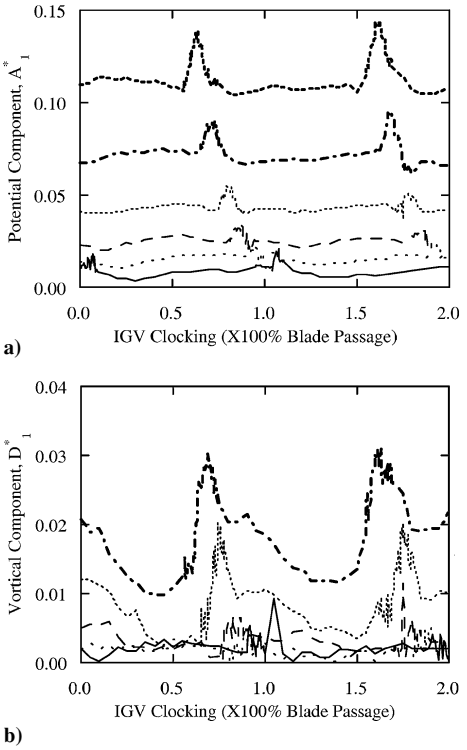

Fig. 23 Time-varying first-harmonic vortical gust magnitude of the rotor for two IGV passages: a) potential: ——, $\xi/S_I = 0.26$, $\xi_u/S_R = 0.85$; - - - -, $\xi/S_I = 0.44$, $\xi_u/S_R = 0.67$; – – –, $\xi/S_I = 0.55$, $\xi_u/S_R = 0.55$; · · · ·, $\xi/S_I = 0.67$, $\xi_u/S_R = 0.43$; ···, $\xi/S_I = 0.78$, $\xi_u/S_R = 0.31$; and – – –, $\xi/S_I = 0.89$, $\xi_u/S_R = 0.19$ and b) vortical: ——, $\xi/S_I = 0.44$, $\xi_u/S_R = 0.67$; - - - -, $\xi/S_I = 0.55$, $\xi_u/S_R = 0.55$; – – –, $\xi/S_I = 0.67$, $\xi_u/S_R = 0.43$; · · · ·, $\xi/S_I = 0.78$, $\xi_u/S_R = 0.31$; and ···, $\xi/S_I = 0.89$, $\xi_u/S_R = 0.19$.

Conclusions

A series of experiments were performed in a high-speed fan stage to investigate and quantify the time-varying characteristics of IGV wakes, including the effect of the downstream rotor potential field. The unsteady velocity and total pressure fields downstream of the IGVs and upstream of the rotor were measured across a single vane passage and time-resolved over one rotor blade passage period for one IGV–rotor axial spacing.

The difference of the maximum and minimum velocity profiles increases, as expected, as the rotor blades are approached due to the increasing rotor potential field. Velocity perturbations increase in the region of the IGV wake due to the effect of the rotor wake chopping the IGV wake. When the rotor blades cut the IGV wake, there are large unsteady pressure fluctuations on the rotor blade, which leads changes in the upstream rotor potential.

Axial velocity deficit increases dramatically when the constructive interaction occurs. When the tangential velocity profile is examined we can see that there is considerable overturning outside the IGV wake and underturning in the IGV wake for the constructive interaction. Note that the flow in the wake region is always toward the hub in the radial velocity profiles. This radially inward flow is a result of an imbalance of the centrifugal and pressure forces near the surface of the blade. Constructive interaction of the wake radial velocity occurs 180-deg out-of-phase with the constructive interaction in the axial and tangential velocity profiles.

The semiwake width for the time-averaged and destructive interaction are in good agreement with each other and all three correlations. As the rotor is approached, the semiwake width for the constructive interaction increases dramatically. The nature of the semiwake width for the axial velocity shown in Fig. 15 is similar in nature to that of the absolute velocity. The velocity deficit of the time-averaged and destructive interaction measured from the absolute velocity is in good agreement with the modified Majjigi-Gliebe correlation[7] and the Lakshminarayana and Davino correlation.[9] The constructive interaction causes larger deficits than either the time-averaged or the destructive interaction. The radial velocity deficit is larger at all axial locations for the constructive interaction.

The potential gust first-harmonic magnitude goes through a complete cycle over one rotor blade pass period. This potential component increases as the rotor is approached due to the increasing magnitude of the rotor potential field. Similarly, the first-harmonic vortical gust magnitude completes one cycle during one rotor blade pass period. The maximum of each curve corresponds the constructive interaction, and the minimum corresponds to the destructive interaction.

The splitting analysis was also applied to the rotor potential field, and the results are a function of the IGV clocking position. Note that the rotor potential field is largest in the region of the IGV wakes, and this is attributed to the rotor blade surface pressure fluctuations, which occur as a result of the IGV wake being cut by the rotor blades. Note that the vortical component is much smaller than the vortical component of the time-varying IGV wake. This effect was found to exist in data taken at lower Mach numbers and at several different IGV–rotor spacings. This indicated that the interaction creates an increase in the apparent vortical component in the IGV wake that can not be attributed to the rotor wake vortical component.

These results indicate the feasibility of affecting performance, forced response, and noise by wake modification with a correctly phased pressure field.

References

[1]Walker, G. J., and Oliver, A. V. R., "The Effect of Interaction Between Wakes from Blade Rows in an Axial Flow Compressor on the Noise Generated by Blade Interaction," *Journal of Engineering for Power*, Vol. 94, 1972, pp. 241–248.

[2]Johnston, R. T., and Fleeter, S., "Airfoil Row Wake Interactions in a High Speed Axial Compressions," *Journal of Propulsion and Power*, Vol. 18, No. 6, 2002, pp. 1280–1288.

[3]Huber, F. W., Johnson, D., Sharma, O. P., Stauback, J. B., and Gaddis, S. W., "Performance Improvement Through Indexing of Turbine Airfoils Part 1—Experimental Investigation," American Society of Mechanical Engineers, ASME Paper 95-GT-27, June 1995.

[4]Sanders, A., and Fleeter, S., "Vane Row Indexing for Passive Vibration Control of Axial Flow Turbomachine Rotors," *Journal of Propulsion and Power*, Vol. 15, No. 5, 1999, pp. 650–658.

[5]Johnston, R. T., and Fleeter, S., "High-Speed Rotor Wake Total Temperature Measurements using a Hot-Film Anemometer," *Experiments in Fluids*, Vol. 25, Sept. 1998, pp. 337–346.

[6]Schmidt, D. P., and Okiishi, T. H., "Multistage Axial-Flow Turbomachine Wake Production, Transport, and Interaction," *AIAA Journal*, Vol. 15, No. 8, 1977, pp. 1138–1145.

[7]Majjigi, R. K., and Gliebe, P. R., "Development of a Rotor Wake/Vortex Model," Vol. 1, Final Rept. NASA CR 174849, 1984, pp. 6–21.

[8]Johnston, R. T., Fleeter, S., "Time Resolved Variations of an IGV Flow Field in the Presence of a Rotor Potential Field," AIAA Paper 96-2670, July 1996.

[9]Lakshminarayana, B., and Davino, R., "Mean Velocity and Decay Characteristics of the Guide Vane and Stator Blade Wake of an Axial Flow Compressor," *Journal of Engineering for Power*, Vol. 102, Jan. 1980, pp. 50–60.

[10]Feiereisen, J. M., and Fleeter, S., "Linear Theory Unsteady Aerodynamics: Low-Solidity Stator Row Response to Combined Vortical/Potential Forcing Functions," AIAA Paper 94-2974, June 1994.

[11]Lui, T., Torgerson, S., Johnston, R., Fleeter, S., and Sullivan, J., "Rotor Blade Pressure Measurement in a High Speed Axial Compressor using Pressure and Temperature Sensitive Paints," *Journal of Propulsion and Power*, Vol. 18, No. 2, 2002, pp. 491–493.